In situ characterization of cofacial Co(IV) centers in Co_4O_4 cubane: Modeling the high-valent active site in oxygen-evolving catalysts

Casey N. Brodsky[a,1], Ryan G. Hadt[b,1], Dugan Hayes[b], Benjamin J. Reinhart[b], Nancy Li[a], Lin X. Chen[b,c], and Daniel G. Nocera[a,2]

[a]Department of Chemistry and Chemical Biology, Harvard University, Cambridge, MA 02138; [b]Chemical Sciences and Engineering Division, Argonne National Laboratory, Lemont, IL 60439; and [c]Department of Chemistry, Northwestern University, Evanston, IL 60208

Contributed by Daniel G. Nocera, February 7, 2017 (sent for review November 23, 2016; reviewed by Kyle M. Lancaster and James K. McCusker)

The Co_4O_4 cubane is a representative structural model of oxidic cobalt oxygen-evolving catalysts (Co-OECs). The Co-OECs are active when residing at two oxidation levels above an all-Co(III) resting state. This doubly oxidized $Co(IV)_2$ state may be captured in a $Co(III)_2(IV)_2$ cubane. We demonstrate that the $Co(III)_2(IV)_2$ cubane may be electrochemically generated and the electronic properties of this unique high-valent state may be probed by in situ spectroscopy. Intervalence charge-transfer (IVCT) bands in the near-IR are observed for the $Co(III)_2(IV)_2$ cubane, and spectroscopic analysis together with electrochemical kinetics measurements reveal a larger reorganization energy and a smaller electron transfer rate constant for the doubly versus singly oxidized cubane. Spectroelectrochemical X-ray absorption data further reveal systematic spectral changes with successive oxidations from the cubane resting state. Electronic structure calculations correlated to experimental data suggest that this state is best represented as a localized, antiferromagnetically coupled $Co(IV)_2$ dimer. The exchange coupling in the cofacial $Co(IV)_2$ site allows for parallels to be drawn between the electronic structure of the Co_4O_4 cubane model system and the high-valent active site of the Co-OEC, with specific emphasis on the manifestation of a doubly oxidized $Co(IV)_2$ center on O–O bond formation.

water splitting | renewable energy | solar-to-fuels | electrocatalysis | oxygen evolution reaction

The overall efficiency of the solar-to-fuels conversion process of water splitting in large part is determined by the overpotential required to drive the oxygen evolution half-reaction (i.e., $2H_2O \rightarrow O_2 + 4H^+ + 4e^-$) (1–3). This half-reaction may be driven at high activity by Earth-abundant catalysts, which are formed by self-assembly upon anodic deposition from buffered cobalt, nickel, and manganese salt solutions (4–10). As determined by in situ structural measurements (11–14), the heterogeneous films consist of aggregates of metalate clusters of molecular dimension. These metalate clusters are ubiquitous and likely the active catalytic species of conventional metal oxide oxygen evolution reaction (OER) catalysts. High-resolution transmission electron microscopy of crystalline cobalt oxides in neutral and alkaline solutions reveals that the surface of the oxide is indeed an amorphous overlayer comprising the metalate clusters (15–18). Electrochemical kinetics (19) and spectroscopic measurements (20, 21) support a mechanism consisting of a minor equilibrium proton-coupled electron transfer process to generate effectively a Co(III)Co(IV) precatalyst, followed by a subsequent oxidation to generate a doubly oxidized state that drives the turnover-limiting O–O bond-forming step (22). Isotope labeling studies of active oxidic cobalt OER catalysts (23, 24) establish direct coupling of oxygens on neighboring sites, thus identifying one path for O–O bond formation from a $Co(IV)_2$ state,

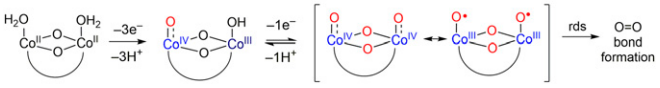

[1]

The generation of the reactive $Co(IV)_2$ intermediate in a minor equilibrium step, followed immediately by rapid catalyst turnover (i.e., O–O bond formation), circumvents its direct observation. In this regard, insights into the details of the OER mechanism in Co-OECs have been greatly aided by molecular model complexes. Complementary electrochemical studies of binuclear cobalt complexes and Co-OECs are consistent with the contention that OER occurs at a dicobalt edge site (23, 25–27). As illustrated in Fig. 1, the edge site geometry of Co-OECs is captured in cobalt cubanes, which are structural analogs of Co-OEC; moreover, stable Co(IV) centers form in cobalt cubanes (2, 21, 28, 29). Although the ligand field of Co_4O_4 cubanes differs slightly from that of Co-OEC arising from the presence of pyridine N and acetate O donors, cobalt-oxo molecular species that stabilize one or more Co(IV) centers are rare. The $Co(III)_3Co(IV)$ state of the cubane has been shown to be a Robin–Day class II mixed-valence (MV) complex (30), and an increase in formal oxidation state to the doubly oxidized cubane has been shown to be active for OER (31, 32). In a $Co_4O_4(py)_4(OAc)_4$ cubane (**1**) (33), the doubly oxidized $Co(III)_2Co(IV)_2$ core may be electrochemically accessed (30). We now report the electron transfer

Significance

The Co-OEC (oxygen-evolving catalyst) is an exemplary OEC that has provided a wealth of kinetics information on the proton-coupled electron transfer mechanism of O–O bond formation. Whereas electrochemical kinetics studies establish a high-valent $Co(IV)_2$ oxidation state as a prerequisite for catalysis, this species cannot be spectroscopically examined in thin-film Co-OECs owing to its short lifetime and dilution against a largely Co(III) background. A molecular model of this high-valent active species is provisioned in the form of a doubly oxidized $Co(III)_2(IV)_2$ cubane. In situ X-ray absorption spectroscopic examination of this high-valent state of the cubane provides direct insights into the electronic structure of a $Co(IV)_2$ site and into its role in the mechanism of O–O bond formation.

Author contributions: C.N.B., R.G.H., and D.G.N. designed research; C.N.B., R.G.H., D.H., and N.L. performed research; C.N.B., R.G.H., D.H., B.J.R., N.L., and L.X.C. contributed new reagents/analytic tools; C.N.B., R.G.H., D.H., N.L., and D.G.N. analyzed data; and C.N.B., R.G.H., and D.G.N. wrote the paper.

Reviewers: K.M.L., Cornell University; and J.K.M., Michigan State University.

The authors declare no conflict of interest.

[1]C.N.B. and R.G.H. contributed equally to this work.

[2]To whom correspondence should be addressed. Email: dnocera@fas.harvard.edu.

This article contains supporting information online at www.pnas.org/lookup/suppl/doi:10.1073/pnas.1701816114/-/DCSupplemental.

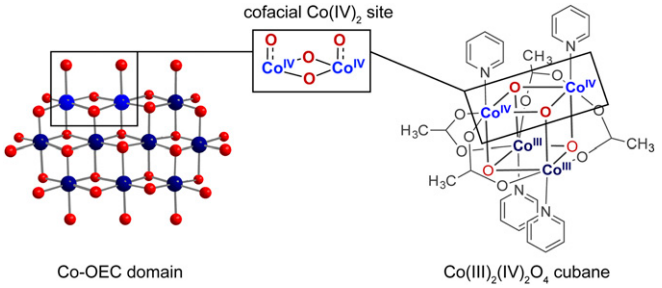

Fig. 1. Cofacial Co(IV)$_2$ sites in Co-OEC are modeled by a Co_4O_4 cubane.

kinetics, in situ optical and X-ray spectroscopies, and density-functional theory (DFT) calculations of the doubly oxidized Co(IV)$_2$ state of the $Co_4O_4(py)_4(OAc)_4$ cubane. These studies provide characterization of a Co(IV)$_2$ state in a molecule and offer direct insight into the role of Co(IV)$_2$ in promoting OER catalysis.

Results

Electrochemistry. Fig. 2*A* shows the cyclic voltammogram (CV) of cubane **1**. Two reversible waves at $E^0(1) = 0.30$ and $E^0(2) = 1.45$ V vs. $Fc^{+/0}$ (all potentials are referenced to ferrocene unless otherwise noted) are observed, corresponding to the Co(III)$_3$(IV)(**1b**)/Co(III)$_4$(**1a**) and Co(III)$_2$(IV)$_2$(**1c**)/Co(III)$_3$(IV)(**1b**) reduction processes. From these potentials, a comproportionation constant of $K_C = 3.05 \times 10^{19}$ is calculated (details in *SI Appendix*) for the equilibrium Co(III)$_4$ + Co(III)$_2$(IV)$_2$ → 2Co(III)$_3$(IV). This large K_C is consistent with the ability to chemically isolate **1b**. The scan rate dependence of the CV of Fig. 2*A* allows for the determination of the electron transfer (ET) kinetics. Fig. 2 *B* and *C* are "trumpet plots" of the experimental CV peak splitting with scan rate (34). The heterogeneous ET rate constant $k_s = 0.110$ and 0.050 cm/s for the first and second oxidations, respectively, may be extracted from simulations of the CVs using DigiElch (35). The fits of the trumpet plots using these k_ss are shown by the solid lines in Fig. 2 *B* and *C*. The difference in rate constants for the two oxidation processes originates from the reorganization energy, λ, comprising inner- (λ_i) and outer-sphere (λ_o) components. The total λ, ascertained from k_s (*SI Appendix*) (36), is λ = 1.00 and 1.08 eV for the oxidation of **1a** and **1b**, respectively.

Spectroelectrochemistry was used to probe the in situ stability of the electrochemically generated doubly oxidized **1c**, as the high standard reduction potential of **1c** precludes its chemical isolation (37). Fig. 3*A* shows the spectral changes accompanying the oxidation of **1a** to **1b** by a constant potential electrolysis (CPE) performed at 0.80 V. The prominent absorption feature of **1a** at 364 nm decreases and a broad increase in absorbance from 400 to 800 nm is observed over the course of oxidation. The spectrum of **1b** was stable under applied potential and isosbestic points are maintained for the conversion. CPE at 1.8 V resulted in the further oxidation of **1b** to **1c**, indicated by a broad growth in absorbance across the entire visible region (Fig. 3*B*). In the absence of applied potential, the spectrum of the **1c** reverts to **1a** over 30 min (*SI Appendix*, Fig. S1).

Isolated samples of **1b** exhibit an intervalence charge-transfer (IVCT) band at ~4,580 cm^{-1} (30). This near-infrared (NIR) absorption is reproduced in the spectroelectrochemical oxidation of **1a** to **1b**, as shown in Fig. 3*C*. An IVCT transition is maintained upon the oxidation of **1b** to **1c**. The IVCT of the in situ, electrochemically generated **1b** is slightly shifted from that of the chemically oxidized species previously reported (30), which may be due to ion pairing effects from electrolyte ions, the presence of trace water in the in situ experiment, incomplete conversion of species within the spectral window, or electric field effects from the Pt flag working electrode. This difference does not preclude a direct comparison between **1b** and **1c** generated under the same conditions in situ. Table 1 lists the ν_{max} and full width at half maximum, $\Delta\nu_{1/2}$, for **1b** and **1c**. The IVCT of **1c** is blue-shifted and has a higher extinction coefficient than that of **1b**. The IVCT transitions were modeled with Gaussian profiles (*SI Appendix*, Fig. S2), and Hush analysis (38–40) permits calculation (*SI Appendix*) of the intramolecular charge-transfer parameters listed in Table 1: H_{ab}, the electronic coupling matrix element between metal centers; λ, the reorganization energy associated with intramolecular ET; ΔG^*, the thermal barrier to intramolecular ET; and k_{ET}, the rate constant of intramolecular ET. Note that the λ determined by IVCT analysis is for a self-exchange ET reaction between Co^{III} and Co^{IV} centers in **1b** and **1c** (λ = 0.7 eV), whereas the λ determined by CV analysis is for the heterogeneous ET reaction describing the one-electron oxidation of Co^{III} to Co^{IV} in **1a** and **1b** (λ = 1.0 eV). The increase in ν_{max} for **1c** compared with **1b** is evidence for an increased λ accompanying double oxidation of the cubane as supported by DFT calculations (*vide infra*). The k_{ET}s are on the order of 10^{12} s^{-1}, consistent with Co(IV) in **1b** appearing delocalized by electron paramagnetic resonance (timescale of ~10^{-9} s) (21) and localized by X-ray absorption spectroscopy (timescale of ~10^{-15} s) (30). In line with this result, the spectroscopy of the oxidized cubanes is consistent with Robin–Day class II mixed valency. Values of the parameter Γ (= $1 - (\Delta\nu_{1/2}/\Delta\nu^0_{1/2})$), where $\Delta\ \nu^0_{1/2}$ is the theoretical

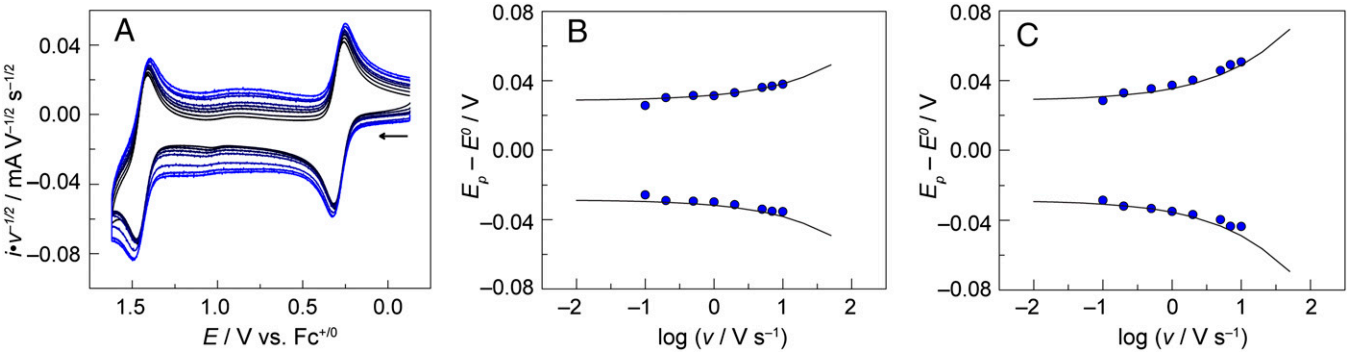

Fig. 2. (*A*) CVs of 1 mM **1** in MeCN + 0.1 M *n*-Bu_4NPF_6 under N_2 on a glassy carbon electrode, at scan rates increasing from $v = 0.1$ (black lines) to 10 (blue lines) V/s. The vertical axis represents current normalized by the square root of the scan rate. (*B*) Trumpet plot of peak splitting of **1a** (blue circles) and fit (black lines), using a heterogeneous electron transfer rate constant of $k_s = 0.110$ cm/s. (*C*) Trumpet plot of peak splitting of **1b** (blue circles) and fit (black lines), using a heterogeneous ET rate constant of $k_s = 0.050$ cm/s.

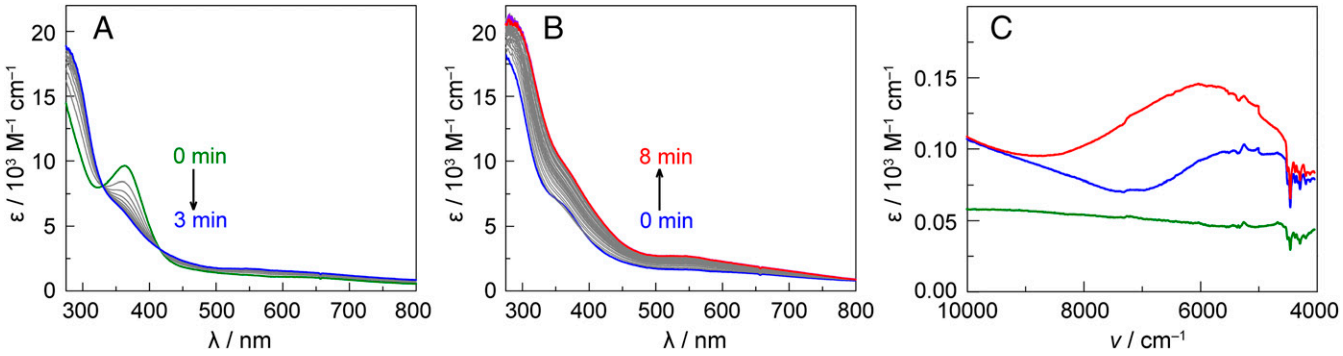

Fig. 3. UV-vis spectroelectrochemistry of the oxidation of (*A*) **1a** (green lines) to **1b** (blue lines) for E_{appl} = 0.80 V vs. $Fc^{+/0}$ and (*B*) **1b** (blue lines) to **1c** (red lines) for E_{appl} = 1.8 V vs. $Fc^{+/0}$. The oxidations were performed on 2 mM MeCN solutions containing 0.1 M *n*-Bu_4NPF_6. (*C*) NIR spectra of **1a** (green lines), **1b** (blue lines), and **1c** (red lines), electrochemically generated at open-circuit potential, 0.80 V, and 1.8 V vs. $Fc^{+/0}$, respectively. NIR spectra were taken on 16.7 mM deuterated MeCN solutions containing 0.1 M *n*-Bu_4NPF_6. Solvent overtones at $\nu < 4{,}000$ cm^{-1} are too intense for an accurate background subtraction. The cell path length for all measurements is 0.05 cm.

bandwidth determined from ν_{max} (*SI Appendix*, Eq. **S8**) between 0 and 0.5, are class II mixed valent, as observed for **1b** and **1c**. Note that the Gaussian fits are partially complicated by the solvent background; however, the fits reported here represent upper bounds on Γ and thus fully support class II behavior and unambiguously rule out class II/III or III behavior.

X-Ray Absorption Spectroscopy. The stability of **1b** and **1c** in spectroelectrochemical experiments allowed their electronic structure to be probed by in situ X-ray absorption spectroscopy (XAS). A 3D-printable X-ray spectroelectrochemical cell was designed and constructed, the details of which will be provided elsewhere (41). We have previously reported the Co K-edge XAS data for powdered samples of **1a** and **1b**, obtained by chemical oxidation of **1a** with cerium ammonium nitrate (30). The Co K-edge XAS data for solutions of **1a** and in situ electrogenerated **1b** are comparable to those of the powdered samples (*SI Appendix*, Fig. S3). In situ Co K-edge spectra for **1a**–**1c** are reproduced in Fig. 4. All spectra show clear edge and preedge features that shift with each subsequent oxidation of the cubane core. The preedge intensity systematically decreases with oxidation (black arrow in the inset), whereas the edge shifts to higher energy upon oxidation. At the position of the blue arrow in Fig. 4, the edge shifts by ∼0.3 eV from **1a** to **1b** and by ∼0.4 eV from **1b** to **1c**. The structure on the rising edge and at the white line, which can include multiple scattering effects, can partially obscure edge shifts in this region of the spectra. This structure is highlighted by first derivative plots of the XAS data given in *SI Appendix*, Fig. S4. Upon formation of **1c**, an additional feature is observed at ∼7716.5 eV, roughly 7 eV above the preedge (red arrow).

DFT Calculations. Broken symmetry (BS) DFT calculations were performed to probe the ground-state electronic structure of **1c** (Fig. 5*A*). The $Co_4O_4(py)_4(OAc)_4$ doubly oxidized cubane was examined with the generalized-gradient approximation functional composed of the Becke 1988 exchange functional and the Perdew 86 correlation functional (BP86) with 15% Hartree–Fock (HF) exchange [B(15HF)P86], which we have previously shown is required to reproduce a localized ground state by partially eliminating the self-interaction error present in pure functionals (30). The $Co(III)_2(IV)_2$ cubane was observed to converge; double oxidation of a single site to produce a $Co(III)_3(V)$ did not converge within the symmetric cubane ligand set. Two possible configurations of **1c** are labeled *cis*-py (∼2.85 Å Co–Co) and *cis*-OAc (∼2.72 Å Co–Co), where the $Co(IV)_2$ dimer can have either two pyridine or two acetate axial ligands, respectively (Fig. 5*A*). Single-point calculations give the lowest energy state as a *cis*-py, localized, antiferromagnetically coupled BS singlet state. The energies of the singlet and triplet states are summarized in Fig. 5*B* for the two configurations, and Mulliken spin densities and population analyses for the α/β-LUMOs (lowest unoccupied molecular orbitals) of the singlet states are given in Table S1. In all cases this analysis supports metal-based oxidation, with largely metal-based hole character and covalent interaction with the oxo ligands and small contributions from pyridine nitrogens and acetate oxygens. The α/β-LUMOs of this $Co(IV)_2$ site are given in Fig. 5*A* (*Left*). The *cis*-py $Co(IV)_2$ triplet is ∼0.9 kcal/mol higher in energy than the BS singlet state ($J \sim -340$ cm^{-1}). The BS singlet state can also be formed in the *cis*-OAc $Co(IV)_2$ dimer, and is ∼0.4 kcal/mol higher in energy than the *cis*-py BS state. The α/β-LUMOs of the *cis*-OAc $Co(IV)_2$ site are given in Fig. 5*A* (*Right*). For *cis*-OAc $Co(IV)_2$, the BS singlet state ($J \sim -19$ cm^{-1}) is nearly isoenergetic with the triplet (ΔE ∼0.05 kcal/mol). In the absence of an experimental measure of *J*, these results are qualitative; nonetheless, the lowest-energy states of *cis*-OAc and *cis*-py are both predicted to be localized, antiferromagnetically coupled $Co(IV)_2$ sites, with the *cis*-py singlet being slightly lower in energy. The magnitude of *J* varies between the two $Co(IV)_2$ sites (∼ –340 vs. –19 cm^{-1} for *cis*-py or *cis*-OAc, respectively) and thus computation predicts that they are thermally accessible. Given their $S_{Tot} = 0$ energies are calculated to be only ∼0.4 kcal/mol different in energy, the singlet states of the two configurations are in thermal equilibrium as well.

Table 1. Thermodynamic and kinetic parameters relevant to intramolecular ET and mixed valency, extracted from Hush analysis of IVCT bands of 1b and 1c

Cubane	ν_{max}, cm^{-1}	$\Delta\nu_{1/2}$, cm^{-1}	$\Delta\nu^0_{1/2}$, cm^{-1}	Γ	H_{ab}, cm^{-1}	λ, eV	ΔG^*, cm^{-1}	k_{ET}, s^{-1}
1b	5,400	2,670	3,530	0.24	273	0.67	1,090	3.22×10^{12}
1c	6,000	3,450	3,720	0.07	394	0.74	1,130	3.17×10^{12}

See *SI Appendix* for Hush calculations.

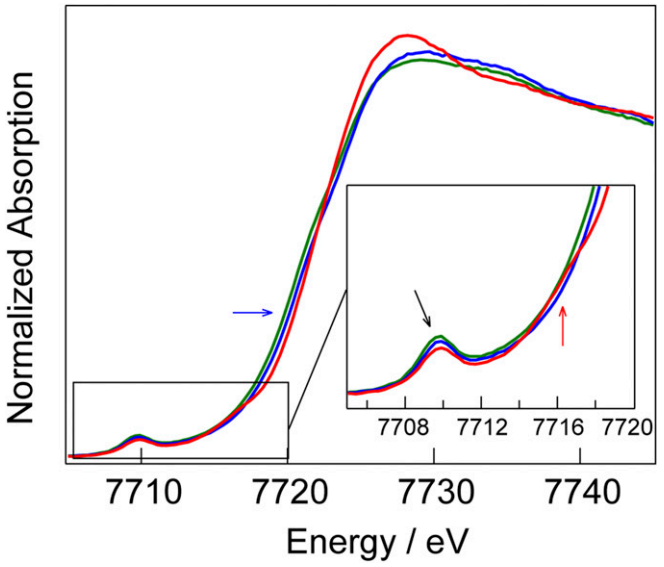

Fig. 4. X-ray spectroelectrochemistry of the three accessible oxidation states of **1**, performed in MeCN + 0.1 M *n*-Bu_4NPF_6. Co K-edge X-ray absorption data for the $Co(III)_4$ (green lines), $Co(III)_3(IV)$ (blue lines), and $Co(III)_2(IV)_2$ (red lines) states, obtained by applying no potential, 0.80, and 1.8 V vs. $Fc^{+/0}$, respectively. Solutions of **1** are 2 mM. The cell path length is 0.1 cm. The blue arrow indicates the position of the edge. The black arrow in the *Inset* indicates the position of the preedge. The red arrow indicates the feature unique to species **1c** at 7716.5 eV.

Discussion

Experimental and computational studies of Co-OEC (19, 23, 24, 42, 43) point to a cofacial oxo-bridged $Co(IV)_2$ site (Fig. 1) as a highly active species poised for turnover-limiting O–O bond formation (Eq. 1). The electronic properties of this highly active binuclear $Co(IV)_2$ site are undefined, as its low concentration in the active catalyst precludes its characterization. To this end, a doubly oxidized Co_4O_4 cubane (**1c**) serves as a competent structural and electronic model of this active site. Electrochemical studies establish the successive oxidation of $Co(III)_4$ to $Co(III)_2(IV)_2$ (Fig. 2), which is supported by XAS data (Fig. 4) showing the presence of a cubane species at a higher Co valency than the known $Co(III)_3(IV)$. A feature ~7 eV above the preedge is unique to the $Co(IV)_2$ state. Important electronic structure characteristics of interest pertaining to the $Co(IV)_2$ site include (*i*) whether the Co(IV)s are localized or delocalized, (*ii*) the nature of the electronic and exchange coupling between the two Co(IV) centers, and the interplay of these two factors.

The presence of Co(IV) and Co(III) centers within the cubane core is indicated by IVCT transitions. With $\Gamma = 0.07$, the IVCT band of **1c** indicates that, like **1b**, it is a class II MV species with localized Co(IV) centers, and the rate constants determined from Hush analysis (Table 1) of the IVCT transitions for **1b** and **1c** establish fast intramolecular Co(IV/III) self-exchange. An analysis of the difference in λ between **1b** and **1c** reveals information about the nature of localization of electron holes in **1c**. Analysis of k_s and the IVCT bands indicate $\lambda(\mathbf{1c}) > \lambda(\mathbf{1b})$. This result is further supported by DFT analysis of the inner-sphere reorganization (λ_i) energy of the cubanes upon ET. For the single-electron oxidation of **1a** to **1b**, $\lambda_i(\mathbf{1b}) = \lambda_a + \lambda_b$, ($\lambda_a$ = E(**1b**)(**1a**) − E(**1b**)(**1b**) and λ_b = E(**1a**)(**1b**) − E(**1a**)(**1a**)), where E(1)(2) (1 designates position 1 and 2 designates position 2) refers to the calculated energy of a molecule in the geometry of (2) and oxidation state of (1) (44, 45). Likewise, $\lambda_i(\mathbf{1c})$ may be determined for the single-electron oxidation of **1b** to **1c**. Using the B(15HF)P86 functional, $\lambda_i(\mathbf{1b})$ ~0.26 eV is obtained using the asymmetrically distorted, localized DFT structure. Conversely, using the symmetrically distorted, delocalized DFT structure, $\lambda_i(\mathbf{1b})$ ~0.14 eV. This decrease in λ_i for valence delocalization is observed in class II vs. III binuclear sites (46) and can be understood from

$$\lambda_i = k_{dis} n (\Delta r)^2, \quad [2]$$

where k_{dis} is the force constant of the distortion coordinate, n is the number of distorting bonds, and Δr is the magnitude of bond distortion upon oxidation. Comparing a valence-localized dimer with a valence-delocalized dimer, n is expected to be halved

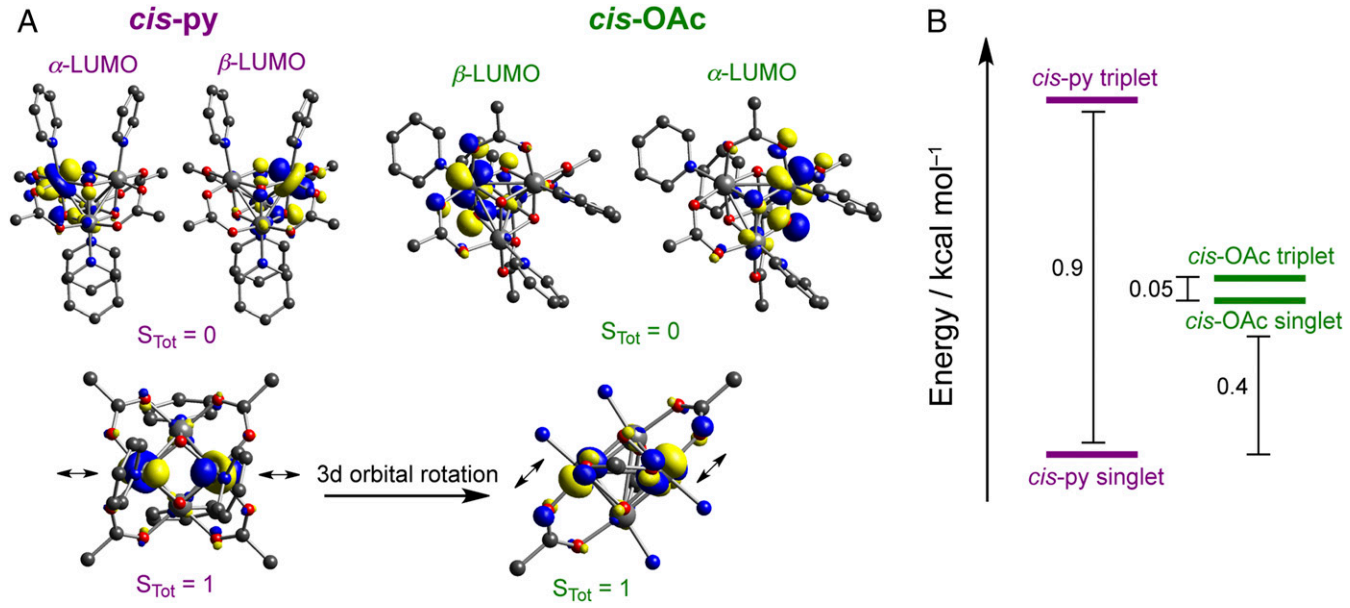

Fig. 5. (*A*) LUMOs of various $Co(III)_2Co(IV)_2$ states. $S_{Tot} = 0$ and 1 states for *cis*-py (*Left*) and *cis*-OAc $Co(IV)_2$ (*Right*). Double-sided arrows in the bottom of the figure indicate 3d-orbital orientations to emphasize relative metal–metal interactions/differential orthogonality (Co, large grey; oxygen, small red; nitrogen, small blue; and carbon, small grey). (*B*) Energy diagram summarizing singlet and triplet energies for the two configurations.

whereas Δr is expected to be doubled ($n_{mon}/n_{dim} \sim 0.5$ and $\Delta r_{mon}/\Delta r_{dim} \sim 2$), so λ_i should be roughly twice as large for a localized oxidation process, assuming similar force constants (46–48). The DFT calculated values of λ_i(**1b**) are in agreement with this prediction, with a reorganization energy for a charge-localized cubane twice that of a charge-delocalized cubane. Moreover, delocalization of charge would not be expected to show a difference in λ_i for Co(IV)s residing on different faces of **1c**. However, localized λ_i(**1c-py**) for the *cis*-py $Co(IV)_2$ site is ~0.28 eV akin to λ_i(**1b**) (~0.26 eV), whereas localized λ_i(**1c-OAc**) for the *cis*-OAc site is ~0.39 eV. The increase of λ_i(**1c-OAc**) by 0.13 eV over λ_i(**1b**) is consistent with the experimentally measured increase of $\Delta\lambda$ = 0.07 eV for **1c** compared with **1b** deduced from IVCT (Table 1) and $\Delta\lambda$ = 0.08 eV deduced from CV kinetics measurements. This finding of localization by DFT is consistent with the outcome of class II IVCT behavior of **1c**.

Localization in **1c** may result from direct Co(IV)–Co(IV) interactions in the form of antiferromagnetic exchange coupling, which can oppose electron–hole delocalization. The exchange coupling of Co(IV) centers in a tetragonal field arises from electrons residing in the t_{2g} derived orbitals, and it may be described by the Heisenberg–Dirac–van Vleck Hamiltonian,

$$\hat{H} = -2JS_AS_B, \quad [3]$$

$$E_{S_{Tot}} = -J[S_{Tot}(S_{Tot}+1) - S_A(S_A+1) - S_B(S_B+1)], \quad [4]$$

where J is the exchange coupling constant, and the total energy, E_{STot}, depends on the total spin state, S_{Tot} = 0 for the singlet ground state and S_{Tot} = 1 for the triplet, which is at an energy $2J$ above the ground state (49). The BS DFT calculations favor antiferromagnetic exchange in **1c**, with $J \sim -340$ cm^{-1} for the *cis*-py $Co(IV)_2$ isomer of **1c** and $J \sim -19$ cm^{-1} for *cis*-OAc $Co(IV)_2$.

The order of magnitude difference in the exchange coupling for *cis*-py $Co(IV)_2$ and *cis*-OAc $Co(IV)_2$ is consistent with structurally unique binuclear $Co(IV)_2$ sites on the faces of the cubane. Whereas the Co–Co distances of ~2.85 and 2.72 Å for *cis*-py and *cis*-OAc isomers, respectively, might suggest a larger J for the latter, the stereoelectronic disposition of the t_{2g} orbitals must be considered. For *cis*-py, the two Co(IV) MOs point directly into the center of the diamond core (Fig. 5, *Left*), maximizing metal–metal overlap and thus promoting strong antiferromagnetic exchange. Due to the different ligand field environment for *cis*-OAc, the two Co(IV) MOs are rotated out of the $Co(IV)_2$ diamond core and are directed toward the Co-oxo bonds (Fig. 5, *Right*), which minimizes metal–metal overlap, mitigating antiferromagnetic exchange. This difference in exchange coupling for *cis*-py and *cis*-OAc suggests that the ligand field in Co-OEC may result in different exchange interactions than present in Co_4O_4; however, the oxo-bridged environment in Co-OEC will likely still favor antiferromagnetic coupling. J is directly related to the electronic coupling matrix element for ET (H_{ab}) (50, 51):

$$-2J = \frac{H_{ab}^2}{U}, \quad [5]$$

where U is the Mott–Hubbard value reflecting intraatomic Coulomb and exchange energies for ET [i.e., Co(IV)Co(IV) → Co(III)Co(V)]. Note H_{ab} in this expression is divided by 2 to account for the reduction of symmetry upon one electron reduction of a binuclear site (50, 51). This expression should be treated qualitatively here, as it is typically used for an authentic dimer, and not a dimer within a tetramer. Using the calculated Js and a U of ~5.5 eV, gives H_{ab}s of ~2,950 and 700 cm^{-1} for the *cis*-py and *cis*-OAc isomers, respectively.

Antiferromagnetic coupling of cofacial $Co(IV)_2$ sites will facilitate O–O bond formation at neighboring metal centers of oxidic cobalt OER catalysts. Such exchange coupling provides a mechanism for charge localization within cubanes, as shown here, and by analogy within the metalate clusters of Co-OEC. Isotope labeling studies of oxidic cobalt OER catalysts (23, 24) and computational mechanistic studies of Co-OECs (42, 43), together with model studies of dicobalt complexes (23), indicate that O–O bond formation requires an adjacent $Co(IV)_2$ active edge site; it is necessary that two Co(IV) centers localize to the edge site of a cobaltate cluster preceding turnover, as opposed to hole equivalents delocalized over the cluster active site. As we show here, antiferromagnetic coupling provides a mechanism to drive hole localization within the cluster core. In addition, exchange coupling offers an adiabatic reaction pathway for O–O bond coupling. Given an edge site Co–Co distance in Co-OEC of 2.82 Å from extended X-ray absorption fine structure (20), the through-space coupling separation is likely similar (i.e., 2.8–2.85 Å). As illustrated in Fig. 6, the exchange-coupled singlet at the metal center may be conveyed to the terminal oxos to form oxyl radicals. This reaction pathway is important within the context of the "oxo wall" (52), which states that a Co(IV)–oxo (Co(IV)=O) will possess significant Co(III)–$O^{\bullet}$ resonance character. Antiferromagnetic coupling may drive O–O bond formation by conveying singlet character to the oxygen radicals to promote direct coupling and bond formation with no spin barrier. This singlet-promoted direct bond formation is analogous to the reverse reaction of O_2 binding to coupled binuclear Cu proteins, where the very strong antiferromagnetic coupling ($-2J \geq 1{,}200$ cm^{-1}) in the side-on (μ-η^2-η^2) peroxo-$Cu(II)_2$ drives the simultaneous two-electron transfer from 2Cu(I) to dioxygen, necessary to overcome the spin-forbidden reaction (53). The ability to generate oxyl radical character dovetails with increasing evidence for the role of oxygen radicals in O–O bond formation by proton-coupled ET (27, 43, 54, 55).

Finally, we note that single-site reactivity has been proposed (31, 56) by further localizing double-oxidizing equivalents on a single Co center to generate a Co(V). In effect, a Co(III)(V) species is a disproportionated $Co(IV)_2$ center. The spectroscopic studies reported here do not support a Co(V) formulation, as the IVCT transition of the doubly oxidized cubane is akin to that of the singly oxidized cubane. Moreover, fast intramolecular ET, in conjunction with the observed electrochemical potentials, suggest that a Co(V) would not be stable in the presence of Co(III) centers. Notwithstanding, a terminal oxo is posited to be a critical determinant for stabilizing a Co(V) center. Such stabilization cannot be achieved in the ligand-saturated cubane examined herein. Accordingly, the spectroscopy of new model cubanes will need to be explored to assess the viability of a fully localized Co(V) active site for OER.

Conclusion

The $Co(III)_2(IV)_2$ state of a Co_4O_4 cubane, $Co_4O_4(py)_4(OAc)_4$, is a faithful structural and electronic model of a $Co(IV)_2$ active site of oxidic cobalt OER catalysts. The $Co(III)_2(IV)_2$ core is furnished electrochemically by oxidation of the $Co(III)_3(IV)$ species; in situ XAS data reflect a cubane core of high Co valency. The stability of an electrochemically generated $Co(III)_2(IV)_2$ cubane engenders more detailed spectroscopic analysis offered by advanced techniques, including in situ X-ray emission where Kβ X-ray emission spectroscopy is sensitive to spin-state (57) and resonant inelastic X-ray scattering. Analysis of the heterogeneous ET rate constant yields a higher reorganization energy for the second oxidation of the cubane core compared with the first. The IVCT bands of both

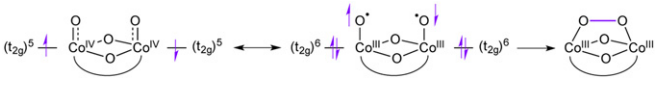

Fig. 6. Electronic considerations for the mechanism of O–O bond formation by intramolecular coupling of oxyl radicals.

the $Co(III)_3(IV)$ and $Co(III)_2(IV)_2$ species are characteristic of Robin–Day class II MV species. DFT calculations indicate greater charge localization within the $Co(III)_2(IV)_2$ core, arising as a direct consequence of antiferromagnetically exchange-coupled Co(IV) sites on a cubane edge. This antiferromagnetic exchange coupling pertains to cobalt oxide catalyzed OER, as exchange coupling localizes charge on the dicobalt site and the metal-centered singlet character may convey singlet character to the generated oxyl radicals, thus providing an adiabatic reaction path for direct O–O coupling.

ACKNOWLEDGMENTS. This material is based upon work supported under the Solar Photochemistry Program of the Chemical Sciences, Geosciences and Biosciences Division, Office of Basic Energy Sciences of the US Department of Energy (D.G.N.) and the Solar Energy Conversion program in Chemical Sciences and Engineering Division at Argonne National Laboratory (ANL) under Contract DE-AC02-06CH11357. R.G.H. is an Enrico Fermi Fellow at ANL and D.H. is a Joseph J. Katz Postdoctoral Fellow at ANL. C.N.B. is a National Science Foundation Graduate Research Fellow at Harvard University. Use of beamline 12BM at the Advanced Photon Source at ANL was supported by the US Department of Energy, Office of Science, Office of Basic Energy Sciences, under Contract DE-AC02-06CH11357.

1. Lewis NS, Nocera DG (2006) Powering the planet: Chemical challenges in solar energy utilization. *Proc Natl Acad Sci USA* 103:15729–15735.
2. Nocera DG (2012) The artificial leaf. *Acc Chem Res* 45:767–776.
3. Surendranath Y, Nocera DG (2011) Oxygen evolution reaction chemistry of oxide–based electrodes. *Prog Inorg Chem* 57:505–560.
4. Kanan MW, Nocera DG (2008) In situ formation of an oxygen-evolving catalyst in neutral water containing phosphate and Co^{2+}. *Science* 321:1072–1075.
5. Huynh M, Bediako DK, Nocera DG (2014) A functionally stable manganese oxide oxygen evolution catalyst in acid. *J Am Chem Soc* 136:6002–6010.
6. Dincă M, Surendranath Y, Nocera DG (2010) Nickel-borate oxygen-evolving catalyst that functions under benign conditions. *Proc Natl Acad Sci USA* 107:10337–10341.
7. Trotochaud L, Young SL, Ranney JK, Boettcher SW (2014) Nickel-iron oxyhydroxide oxygen-evolution electrocatalysts: The role of intentional and incidental iron incorporation. *J Am Chem Soc* 136:6744–6753.
8. Smith RDL, Prévot MS, Fagan RD, Trudel S, Berlinguette CP (2013) Water oxidation catalysis: Electrocatalytic response to metal stoichiometry in amorphous metal oxide films containing iron, cobalt, and nickel. *J Am Chem Soc* 135:11580–11586.
9. Song F, Hu X (2014) Ultrathin cobalt-manganese layered double hydroxide is an efficient oxygen evolution catalyst. *J Am Chem Soc* 136:16481–16484.
10. Qiu Y, Xin L, Li W (2014) Electrocatalytic oxygen evolution over supported small amorphous Ni-Fe nanoparticles in alkaline electrolyte. *Langmuir* 30:7893–7901.
11. Farrow CL, Bediako DK, Surendranath Y, Nocera DG, Billinge SJL (2013) Intermediate-range structure of self-assembled cobalt-based oxygen-evolving catalyst. *J Am Chem Soc* 135:6403–6406.
12. Liu Y, Nocera DG (2014) Spectroscopic studies of nanoparticulate thin films of a cobalt-based oxygen evolution catalyst. *J Phys Chem C* 118:17060–17066.
13. Du P, Kokhan O, Chapman KW, Chupas PJ, Tiede DM (2012) Elucidating the domain structure of the cobalt oxide water splitting catalyst by X-ray pair distribution function analysis. *J Am Chem Soc* 134:11096–11099.
14. Huynh M, Shi C, Billinge SJL, Nocera DG (2015) Nature of activated manganese oxide for oxygen evolution. *J Am Chem Soc* 137:14887–14904.
15. Lee SW, et al. (2012) The nature of lithium battery materials under oxygen evolution reaction conditions. *J Am Chem Soc* 134:16959–16962.
16. Friebel D, et al. (2013) On the chemical state of Co oxide electrocatalysts during alkaline water splitting. *Phys Chem Chem Phys* 15:17460–17467.
17. Bergmann A, et al. (2015) Reversible amorphization and the catalytically active state of crystalline Co_3O_4 during oxygen evolution. *Nat Commun* 6:8625.
18. González-Flores D, et al. (2015) Heterogeneous water oxidation: Surface activity versus amorphization activation in cobalt phosphate catalysts. *Angew Chem Int Ed Engl* 54:2472–2476.
19. Surendranath Y, Kanan MW, Nocera DG (2010) Mechanistic studies of the oxygen evolution reaction by a cobalt-phosphate catalyst at neutral pH. *J Am Chem Soc* 132:16501–16509.
20. Kanan MW, et al. (2010) Structure and valency of a cobalt-phosphate water oxidation catalyst determined by in situ X-ray spectroscopy. *J Am Chem Soc* 132:13692–13701.
21. McAlpin JG, et al. (2010) EPR evidence for Co(IV) species produced during water oxidation at neutral pH. *J Am Chem Soc* 132:6882–6883.
22. Bediako DK, Ullman AM, Nocera DG (2016) Catalytic oxygen evolution by cobalt oxido thin films. *Top Curr Chem* 371:173–213.
23. Ullman AM, Brodsky CN, Li N, Zheng S-L, Nocera DG (2016) Probing edge site reactivity of oxidic cobalt water oxidation catalysts. *J Am Chem Soc* 138:4229–4236.
24. Koroidov S, Anderlund MF, Styring S, Thapper A, Messinger J (2015) First turnover analysis of water-oxidation catalyzed by Co-oxide nanoparticles. *Energy Environ Sci* 8:2492–2503.
25. Costentin C, Porter TR, Savéant J-M (2016) Conduction and reactivity in heterogeneous-molecular catalysis: New insights in water oxidation catalysis by phosphate cobalt oxide Films. *J Am Chem Soc* 138:5615–5622.
26. Zhang M, Frei H (2014) Towards a molecular level understanding of the multi-electron catalysis of water oxidation on metal oxide surfaces. *Catal Lett* 145:420–435.
27. Zhang M, de Respinis M, Frei H (2014) Time-resolved observations of water oxidation intermediates on a cobalt oxide nanoparticle catalyst. *Nat Chem* 6:362–367.
28. Kanan MW, Surendranath Y, Nocera DG (2009) Cobalt-phosphate oxygen-evolving compound. *Chem Soc Rev* 38:109–114.
29. McAlpin JG, et al. (2011) Electronic structure description of a $[Co(III)_3Co(IV)O_4]$ cluster: A model for the paramagnetic intermediate in cobalt-catalyzed water oxidation. *J Am Chem Soc* 133:15444–15452.
30. Hadt RG, et al. (2016) X-ray spectroscopic characterization of Co(IV) and metal-metal interactions in Co_4O_4: Electronic structure contributions to the formation of high-valent states relevant to the oxygen evolution reaction. *J Am Chem Soc* 138:11017–11030.
31. Nguyen AI, et al. (2015) Mechanistic investigations of water oxidation by a molecular cobalt oxide analogue: Evidence for a highly oxidized intermediate and exclusive terminal oxo participation. *J Am Chem Soc* 137:12865–12872.
32. Smith PF, et al. (2015) Water oxidation by the $[Co_4O_4(OAc)_4(py)_4]^+$ cubium is initiated by OH^- addition. *J Am Chem Soc* 137:15460–15468.
33. Chakrabarty R, Bora SJ, Das BK (2007) Synthesis, structure, spectral and electrochemical properties, and catalytic use of cobalt(III)-oxo cubane clusters. *Inorg Chem* 46:9450–9462.
34. Savéant J-M (2006) *Elements of Molecular and Biomolecular Electrochemistry: An Electrochemical Approach to Electron Transfer Chemistry* (John Wiley, Hoboken, NJ), pp 28–62.
35. Rudolph M (2003) Digital simulations on unequally spaced grids: Part 2. Using the box method by discretisation on a transformed equally spaced grid. *J Electroanal Chem* 543:23–39.
36. Costentin C, Louault C, Robert M, Rogé V, Savéant J-M (2012) Reorganization energy and pre-exponential factor from temperature-dependent experiments in electron transfer reactions. A typical example: The reduction of tert-nitrobutane. *Phys Chem Chem Phys* 14:1581–1584.
37. Connelly NG, Geiger WE (1996) Chemical redox agents for organometallic chemistry. *Chem Rev* 96:877–910.
38. Brunschwig BS, Creutz C, Sutin N (2002) Optical transitions of symmetrical mixed-valence systems in the Class II-III transition regime. *Chem Soc Rev* 31:168–184.
39. Kubiak CP (2013) Inorganic electron transfer: Sharpening a fuzzy border in mixed valency and extending mixed valency across supramolecular systems. *Inorg Chem* 52:5663–5676.
40. Brunschwig BS, Sutin N (2001) Reflections on the two-state electron-transfer model. *Electron Transfer in Chemistry*, ed Balzani V (Wiley-VCH, New York), Vol 2, pp 583–615.
41. Reinhart BJ, Hadt RG (2017) A 3D printable sample cell for in situ electrochemical X-ray spectroscopy. To be published.
42. Li X, Siegbahn PEM (2013) Water oxidation mechanism for synthetic Co-oxides with small nuclearity. *J Am Chem Soc* 135:13804–13813.
43. Wang L-P, Van Voorhis T (2011) Direct-coupling O_2 bond forming a pathway in cobalt oxide water oxidation catalysts. *J Phys Chem Lett* 2:2200–2204.
44. Olsson MHM, Ryde U, Roos BO (1998) Quantum chemical calculations of the reorganization energy of blue-copper proteins. *Protein Sci* 7:2659–2668.
45. Ryde U, Olsson MHM (2001) Structure, strain, and reorganization energy of blue copper models in the protein. *Int J Quantum Chem* 81:335–347.
46. Gamelin DR, et al. (1998) Spectroscopy of mixed-valence Cu_A-type centers:Ligand-field control of ground-state properties related to electron transfer. *J Am Chem Soc* 120:5247–5263.
47. Bominaar EL, Achim C, Borshch SA, Girerd JJ, Münck E (1997) Analysis of exchange interaction and electron delocalization as intramolecular determinants of intermolecular electron-transfer kinetics. *Inorg Chem* 36:3689–3701.
48. Larsson S, Källebring B, Wittung P, Malmström BG (1995) The Cu_A center of cytochrome-c oxidase: Electronic structure and spectra of models compared to the properties of Cu_A domains. *Proc Natl Acad Sci USA* 92:7167–7171.
49. van Vleck JH (1965) *The Theory of Electric and Magnetic Susceptibilities* (Oxford Univ Press, London).
50. Brunold TC, Gamelin DR, Solomon EI (2000) Excited-state exchange coupling in bent Mn(III)–O–Mn(III) complexes: Dominance of the π/σ superexchange pathway and its possible contributions to the reactivities of binuclear metalloproteins. *J Am Chem Soc* 122:8511–8523.
51. Tuczek F, Solomon EI (2001) Excited electronic states of transition-metal dimers and the VBCI model: An overview. *Coord Chem Rev* 219–221:1075–1112.
52. Winkler J, Gray H (2012) Electronic structures of oxo-metal ions. *Molecular Electronic Structures of Transition Metal Complexes I, Structure and Bonding*, eds Mingos DMP, Day P, Dahl JP (Springer, Berlin), Vol 142, pp 17–28.
53. Solomon EI, et al. (2014) Copper active sites in biology. *Chem Rev* 114:3659–3853.
54. Yang X, Baik MH (2006) cis,cis-[(bpy)2RuVO]2O4+ catalyzes water oxidation formally via in situ generation of radicaloid RuIV-O. *J Am Chem Soc* 128:7476–7485.
55. Jiang Y, et al. (2013) Promoting the activity of catalysts for the oxidation of water with bridged dinuclear ruthenium complexes. *Angew Chem Int Ed Engl* 52:3398–3401.
56. Mattioli G, Giannozzi P, Amore Bonapasta A, Guidoni L (2013) Reaction pathways for oxygen evolution promoted by cobalt catalyst. *J Am Chem Soc* 135:15353–15363.
57. Glatzel P, Bergmann U (2005) High resolution 1s core hole X-ray spectroscopy in 3d transition metal complexes—electronic and structural information. *Coord Chem Rev* 249:65–95.